

Transits and starspots in the WASP-6 planetary system

Jeremy Tregloan-Reed,^{1,2*} John Southworth,² M. Burgdorf,³ S. Calchi Novati,^{4,5,6}
M. Dominik,^{7†} F. Finet,^{8,9} U. G. Jørgensen,¹⁰ G. Maier,¹¹ L. Mancini,¹² S. Prof,¹¹
D. Ricci,^{13,14,15} C. Snodgrass,¹⁶ V. Bozza,^{5,17} P. Browne,⁷ P. Dodds,⁷ T. Gerner,¹¹
K. Harpsøe,¹⁰ T. C. Hinse,^{18,19} M. Hundertmark,⁷ N. Kains,²⁰ E. Kerins,²¹ C. Liebig,⁷
M. T. Penny,²² S. Rahvar,²³ K. Sahu,²⁰ G. Scarpetta,^{5,6,17} S. Schäfer,²⁴
F. Schönebeck,¹¹ J. Skottfelt¹⁰ and J. Surdej⁸

Affiliations are listed at the end of the paper

Accepted 2015 March 30. Received 2015 March 27; in original form 2014 February 20

ABSTRACT

We present updates to PRISM, a photometric transit-starspot model, and GEMC, a hybrid optimization code combining MCMC and a genetic algorithm. We then present high-precision photometry of four transits in the WASP-6 planetary system, two of which contain a starspot anomaly. All four transits were modelled using PRISM and GEMC, and the physical properties of the system calculated. We find the mass and radius of the host star to be $0.836 \pm 0.063 M_{\odot}$ and $0.864 \pm 0.024 R_{\odot}$, respectively. For the planet, we find a mass of $0.485 \pm 0.027 M_{\text{Jup}}$, a radius of $1.230 \pm 0.035 R_{\text{Jup}}$ and a density of $0.244 \pm 0.014 \rho_{\text{Jup}}$. These values are consistent with those found in the literature. In the likely hypothesis that the two spot anomalies are caused by the same starspot or starspot complex, we measure the stars rotation period and velocity to be 23.80 ± 0.15 d and 1.78 ± 0.20 km s⁻¹, respectively, at a colatitude of 75.8°. We find that the sky-projected angle between the stellar spin axis and the planetary orbital axis is $\lambda = 7.2^{\circ} \pm 3.7^{\circ}$, indicating axial alignment. Our results are consistent with and more precise than published spectroscopic measurements of the Rossiter–McLaughlin effect. These results suggest that WASP-6 b formed at a much greater distance from its host star and suffered orbital decay through tidal interactions with the protoplanetary disc.

Key words: techniques: photometric – stars: fundamental parameters – stars: individual: WASP-6 – planetary systems – starspots.

1 INTRODUCTION

At present¹ a total of 1890 planets outside of our own Solar system are listed in the authoritative catalogue of Schneider et al. (2011). Of these, approximately two-thirds have been discovered from ground-based (e.g. SuperWasp: Pollacco et al. 2006; HAT: Bakos et al. 2004) or space-based (*CoRoT*: Baglin et al. 2006; *Kepler*: Borucki et al. 2010) transit surveys, and later confirmed by use of the radial velocity (RV) technique (Butler et al. 1996, 1999; Queloz et al. 2000). Many more candidate exoplanets have been listed in the literature, mainly from the *Kepler* satellite survey which has also detected several Earth-size planets in the habitable zone of their

parent star, indicating new worlds with mass and size similar to our own Earth (Borucki et al. 2012, 2013).

During a planetary transit, the planet follows a path (called the transit chord) across the surface of the stellar disc and can be used to probe changes in brightness on the stellar surface (Silva 2003). Starspots have different temperatures to the surrounding photosphere, so emit a different amount of flux. Because photometry measures the change in intensity as a function of time, the occultation of a starspot by the planet causes an anomaly in the light curve (Silva 2003). The anomaly is either an increase or decrease in the amount of light received from the star. If the starspot is a cool spot, then the amount of light will increase when the planet crosses the starspot (Pont et al. 2007; Rabus et al. 2009; Winn et al. 2010b). If the starspot is a hotspot (e.g. a facula), then the amount of light will reduce when the planet occults the spot.

At present, when a light curve of a transiting exoplanet is observed to have a starspot anomaly, the transit and the spot are generally modelled separately (e.g. Désert et al. 2011; Maciejewski

*E-mail: jeremy.j.tregloan-reed@nasa.gov

†Royal Society University Research Fellow.

¹ (<http://exoplanet.eu>) accessed on 2015/02/20

et al. 2011; Nutzman, Fabrycky & Fortney 2011; Sanchis-Ojeda et al. 2011). First, a transit model is fitted to the data points not affected by the starspot anomaly. Then the spot-affected residuals versus the best-fitting model are modelled using a Gaussian function (e.g. Sanchis-Ojeda & Winn 2011; Sanchis-Ojeda et al. 2011). This method neglects the fact that the starspot affects the entire transit shape and not just the section where the planet crosses the spot (Ballerini et al. 2012). Carter et al. (2011) use the idea that a starspot on the stellar disc will affect the transit depth to explain the observed changes in transit depth for GJ 1214. This is due to the change in the star’s brightness in its long-term light curve due to starspots rotating on and off the stellar disc.

The transit depth is not the only property of a transit light curve that the starspot affects, it also affects the determination of the measured stellar mean density, stellar radius, orbital inclination and limb darkening (LD) coefficients (Ballerini et al. 2012). The LD coefficients depend on wavelength: because a starspot has a different temperature compared to the surrounding photosphere, it has a different spectral energy distribution and thus different LD coefficients. Therefore, the application of an LD law with a single set of coefficients to the entire stellar surface causes a bias in the modelling process (Ballerini et al. 2012). The difference in LD coefficients between the spot and the photosphere can be as much as 30 per cent in the UV. The effects on the measured stellar radius and orbital inclination of the system are artefacts from errors in the measured planetary radius, which is derived from the transit depth. A change in the measured planetary radius must be compensated for by a change in the measured stellar radius or semimajor axis in order to retain the same transit duration. Starspots can also affect the measured transit mid-point (Sanchis-Ojeda et al. 2011; Barros et al. 2013) and create false positives in transit timing measurements. Sanchis-Ojeda et al. (2011) calculated that a starspot anomaly in a transit of WASP-4 with an amplitude of 0.3–0.5 mmag could produce a timing noise of five to ten seconds.

1.1 Introducing WASP-6

The transiting planetary system WASP-6 was discovered by Gillon et al. (2009) using photometry from the WASP-South telescope. They determined an orbital period of $P = 3.361$ d for the planet WASP-6 b. Dedicated photometric observations were then performed in the i' band using the 2-m Faulkes Telescope South (FTS) and in a broad $V+R$ band using the RISE instrument (Steele et al. 2008) on the 2-m Liverpool Telescope.

RV measurements were obtained using two spectrographs: CORALIE on the 1.2-m Euler telescope (Baranne et al. 1996; Queloz et al. 2000) and HARPS on the ESO 3.6-m telescope (Mayor et al. 2003). Gillon et al. (2009) determined the stellar mass and radius to be $M_* = 0.88^{+0.05}_{-0.08} M_\odot$ and $R_* = 0.870^{+0.025}_{-0.036} R_\odot$, respectively. They found the planetary mass and radius to be $M_p = 0.503^{+0.019}_{-0.038} M_{\text{Jup}}$ and $R_p = 1.224^{+0.051}_{-0.052} R_{\text{Jup}}$. They also determined a value for the projected stellar rotational velocity of $v \sin I = 1.4 \pm 1.0$ km s⁻¹ from measurements of line widths in the HARPS spectra with a macroturbulence (v_{mac}) value of 2 km s⁻¹. They noted that if a value of $v_{\text{mac}} = 0$ km s⁻¹ is used then $v \sin I = 3.0 \pm 0.5$ km s⁻¹, while if v_{mac} became slightly larger than 2 km s⁻¹ then $v \sin I$ would drop to zero. From their RVs, Gillon et al. (2009) measured the Rossiter–McLaughlin (RM) effect. They found that the system is in alignment with a sky-projected spin orbit alignment, $\lambda = 11^{+14}_{-18}$ deg.

The spectral analysis of 11 WASP host stars by Doyle et al. (2013) included WASP-6 A. Doyle et al. (2013) derived new

values for the stellar mass and radius of $M_* = 0.87 \pm 0.06 M_\odot$ and $R_* = 0.77 \pm 0.07 R_\odot$, in agreement with those of Gillon et al. (2009). Doyle et al. (2013) determined $v_{\text{mac}} = 1.4 \pm 0.3$ km s⁻¹ and $v \sin I = 2.4 \pm 0.5$ km s⁻¹, and an effective temperature of $T_{\text{eff}} = 5375 \pm 65$ K.

An optical transmission spectrum for WASP-6 has been constructed using multi-object differential spectrophotometry with the IMACS spectrograph on the Magellan Baade telescope (Jordán et al. 2013). The observations comprised of 91 spectra covering 480–860 nm. The analysis yielded a mostly featureless transmission spectrum with evidence of atmospheric hazes and condensates. Most recently, Nikolov et al. (2015) used the *Hubble Space Telescope* to perform transmission spectroscopy of WASP-6, and found a haze in the atmosphere of WASP-6 b. They also determined a rotational modulation of $P_{\text{rot}} = 23.6 \pm 0.5$ d for WASP-6 A.

2 UPDATES TO PRISM AND GEMC

A code written in IDL² called PRISM (planetary retrospective integrated starspot model) was developed to model a starspot anomaly in transit light curves of WASP-19 (see Tregloan-Reed, Southworth & Tappert 2013). PRISM uses a pixellation approach to represent the star and planet on a two-dimensional array in Cartesian coordinates. This makes it possible to model the transit, LD and starspots on the stellar disc simultaneously. LD was implemented using the standard quadratic law. PRISM uses the 10 parameters given in Table 1 to model the system, where the fractional stellar and planetary radii are defined as the absolute radii scaled by the semimajor axis ($r_{*,p} = R_{*,p}/a$).

A new optimization algorithm called GEMC (Genetic Evolution Markov Chain) was also created alongside PRISM to help improve the efficiency of finding a global solution in a rugged parameter space compared to conventional MCMC algorithms (Tregloan-Reed et al. 2013). GEMC is a hybrid between an MCMC and a genetic algorithm³ and is based on the Differential Evolution Markov Chain (DE-MC) put forward by Ter Braak (2006). During the ‘burn-in’ stage GEMC runs N chains in parallel and for every generation each chain is perturbed in a vector towards the current best-fitting chain. Once the burn-in stage has been completed, GEMC switches to a conventional MCMC algorithm (each chain used in the burn-in begins independent MCMC runs) to determine the parameter uncertainties (see Tregloan-Reed et al. 2013).

Since the development of both PRISM and GEMC, other authors have used the codes to not only help ascertain the photometric parameters of a transiting system but to also derive the parameters of the starspots observed in transit light curves (e.g. Mancini et al. 2013, 2014; Mohler-Fischer et al. 2013). Béky, Kipping & Holman (2014) used PRISM to help calibrate their semi-analytic transit-starspot model SPOTROD.

Before using both PRISM and GEMC in modelling the WASP-6 system, it was decided to make a few improvements.⁴ The original version of PRISM assumed a circular orbit, as most transiting planets either have a circular orbit or lack a measurement of the orbital

² The acronym IDL stands for Interactive Data Language and is a trademark of Exelis Visual Information Solutions. For further details see <http://www.exelisvis.com/ProductsServices/IDL.aspx>.

³ A genetic algorithm mimics biological processes by spawning successive generations of solutions based on breeding and mutation operators from the previous generation.

⁴ The new versions of both PRISM and GEMC are available from <http://www.astro.keele.ac.uk/~jtr>

Table 1. Original and recovered parameters from a simulated transit light curve using either 15 or 50 pixels for the planetary radius, plus the interval within which the best fit was searched for using GEMC.

Parameter	Symbol	Original value	Search interval	Recovered value $r_p = 50$ pixels	Recovered value $r_p = 15$ pixels
Radius ratio	r_p/r_*	0.15	0.05–0.30	0.1496 ± 0.0013	0.1498 ± 0.0011
Sum of fractional radii	$r_s + r_p$	0.25	0.10–0.50	0.2486 ± 0.0024	0.2512 ± 0.0026
Linear LD coefficient	u_1	0.3	0.0–1.0	0.291 ± 0.104	0.281 ± 0.114
Quadratic LD coefficient	u_2	0.2	0.0–1.0	0.192 ± 0.042	0.189 ± 0.039
Orbital inclination (deg)	i	85.0	70.0–90.0	85.16 ± 0.46	85.29 ± 0.44
Transit epoch (Phase)	T_0	0.015	−0.50 to 0.50	$0.014\ 94 \pm 0.000\ 11$	$0.015\ 02 \pm 0.000\ 10$
Longitude of spot (deg)	θ	30.0	−90.0 to +90.0	30.50 ± 1.17	30.47 ± 1.21
Colatitude of spot (deg)	ϕ	65.0	0.0–90.0	64.51 ± 5.83	64.17 ± 5.55
Spot angular radius (deg)	r_{spot}	12.0	0.0–30.0	12.73 ± 2.00	12.33 ± 1.87
Spot contrast	ρ_{spot}	0.8	0.0–1.0	0.797 ± 0.057	0.781 ± 0.061

eccentricity. However, Gillon et al. (2009) found that the orbit of WASP-6 b has a small orbital eccentricity of $e = 0.054^{+0.018}_{-0.015}$, with an argument of periastron $\omega = 97.4^{+6.9}_{-13.2}$ deg. As a consequence, PRISM was extended to allow for eccentric orbits. e and ω have been set to roam within the physically bounded ranges of $0 \leq e \leq 1$ and $0^\circ \leq \omega \leq 360^\circ$. A Gaussian prior is used to help constrain the parameter values close to the expected values found in the literature. The logic behind using a Gaussian prior stems from the fact that it is not possible to ascertain these values from photometry alone (due to only observing a small fraction of the orbit) unless an occultation is observed (Kipping et al. 2012). Because we have the knowledge of where the values of e and ω should lie and that they have an effect on the other system parameters (in particular i and r_*), it is imperative to examine every potential solution selected from a Gaussian probability distribution of e and ω to accurately estimate the uncertainties in all of the other system parameters.

It was shown by both Silva-Valio et al. (2010) and Mohler-Fischer et al. (2013) that in some cases there can be more than one starspot anomaly in a single transit light curve. While PRISM was originally designed to model multiple starspots, the static coding of GEMC made it only possible to fit for either a single starspot or a spot-free stellar surface. To facilitate further work, GEMC was modified to fit for multiple starspots. This was accomplished by allowing the initial reading of the input file to be dynamic, so GEMC can determine the number of starspots to be fitted based on the number of parameters used. This can be done by adding multiple spot parameter ranges in the input file. It is possible to fix the position of a starspot and therefore assign starspots to sections of the stellar disc where they will not be occulted by the planet, thus allowing investigations of the effects of unocculted starspot on transit light curves.

PRISM was designed to use the pixellation approach, and to maintain numerical resolution was hard coded to set the planetary radius at 50 pixels. The host star’s radius in pixels was scaled accordingly based on the input parameters. The new version now allows users to set the size of the planetary radius in pixels. This makes it possible to reduce the amount of time required to complete each model iteration, at the cost of numerical resolution (see Section 2.1 for more details). In tests using a planet radius set at 15 pixels, it took PRISM and GEMC approximately 13 s to model a single generation of 256 solutions using synthetic data, which equates to approximately 0.05 s per iteration. For comparison, a planetary radius of 50 pixels results in approximately 0.47 s per iteration.⁵

To increase the efficiency of determining the parameter uncertainties, the MCMC component of GEMC was replaced with DE-MC (Ter Braak 2006). DE-MC combines the genetic algorithm DE (Price & Storn 1997; Storn & Price 1997) with MCMC. The combination of DE and MCMC is used to solve a problem in MCMC by determining the orientation and the scale of the step sizes. Adaptive directional sampling in MCMC does solve the orientation problem, but not the scale (Ter Braak 2006). DE-MC works by creating a population of MCMC chains whose starting points are initialized from overdispersed states and instead of letting the chains run independently and checking for convergence (e.g. Gelman & Rubin 1992) they are instead run in parallel and learn from each other. The perturbation steps taken by each chain are given by equation (1). Assuming a d -dimensional parameter space and using N chains then the population \mathbf{X} is a $N \times d$ matrix, with the chains labelled $\mathbf{x}_1, \mathbf{x}_2, \dots, \mathbf{x}_N$. Therefore, the proposal vector \mathbf{x}_p is generated by

$$\mathbf{x}_p = \mathbf{x}_i + \gamma (\mathbf{x}_{R1} - \mathbf{x}_{R2}) + \mathbf{e}, \quad (1)$$

where \mathbf{x}_i is the current i th chain, γ is the scale factor calculated from $\gamma = 2.4/\sqrt{2d}$ (Ter Braak 2006), \mathbf{x}_{R1} and \mathbf{x}_{R2} are two randomly selected chains and \mathbf{e} is drawn from a symmetric distribution with a small variance compared to that of the target. \mathbf{x}_p is then tested for fitness and if accepted it is used as the next step in \mathbf{x}_i .

After the ‘burn in’ stage of an MCMC chain, determining the required step size to allow a 20–25 per cent acceptance rate can be difficult. For a transit light curve altering the orbital inclination, i , by 0.05 per cent should only cause a small increase in χ^2 but a 0.05 per cent alteration in the transit mid-point, T_0 , could cause a large increase in χ^2 . DE-MC overcomes the problem with the scale of the step sizes by using the clustering of the chains around the global solution after the ‘burn in’: the difference vector between two randomly selected chains will contain the individual scale for each parameter (e.g. 0.05 per cent for i and 0.000 01 per cent for T_0). Ter Braak (2006) argues that DE-MC is a single N chain that is simply a single random walk Markov Chain in a $N \times d$ dimensional space.

The use of DE-MC in the exoplanet community is increasing, especially for models involving a large number of parameters. For example, models of transiting circumbinary planets can contain over 30 parameters (e.g. Doyle et al. 2011; Orosz et al. 2012; Welsh et al. 2012; Schwamb et al. 2013). To accurately estimate the parameter uncertainties, the MCMC component of GEMC required 10^6 function iterations (10 chains each of 10^5 steps). The DE-MC component requires approximately 2×10^5 function iterations (128 chains each of 1500 steps; e.g. Welsh et al. 2012). This equates to a five-fold reduction in the amount of computing time required to fit a transit light curve. When using a set of synthetic transit data, it took GEMC

⁵ These tests were performed on a 2.4 GHz quad-core laptop.

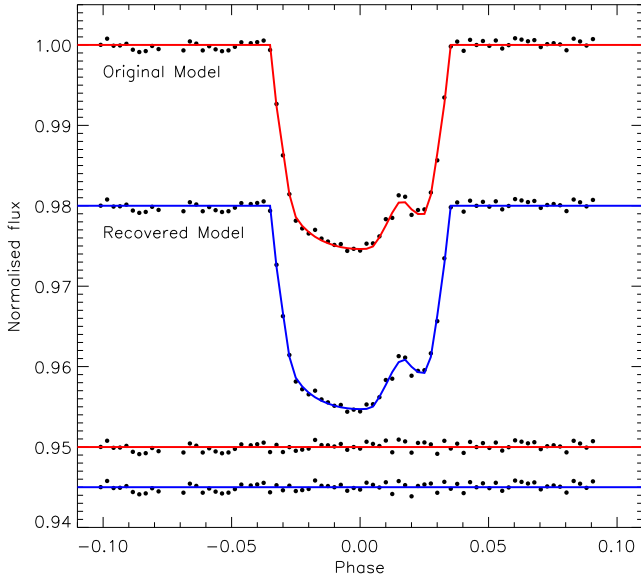


Figure 1. Recovered and original models to simulated transit data created by PRISM and recovered by GEMC and PRISM. The residuals are shown at the bottom. The model was calculated with $r_p = 50$ pixels.

approximately 5.4 d to fit the data using a planet radius of 50 pixels coupled with the MCMC component. The use of a planet radius of 15 pixels combined with the DE-MC algorithm resulted in GEMC taking only 2.7 h to fit the same data.

2.1 Forward simulation of synthetic data

The modifications to PRISM and GEMC were validated by modelling simulated transit data containing a starspot anomaly. For this test, PRISM was used to create multiple simulated transits with a range of parameters. Noise was then added to the light curves so that the rms scatter between the original simulated light curves and the light curves with added noise was ≈ 500 ppm. Other levels of noise were also used in similar tests. This was to approximate a realistic level of noise found in transit light curves observed using the defocused photometry technique. Error bars were then assigned to each data point to give the original noise-free model a reduced chi-squared value of $\chi^2_v = 1$.

Once a simulated transit light curve had been created, GEMC and PRISM were used in an attempt to recover the initial input parameters. Different values for the planetary pixel radius were also used to test for numerical resolution. Table 1 shows the results for one of the tests using both $r_p = 50$ and $r_p = 15$ pixels, while Fig. 1 shows the simulated transit light curve together with the original and recovered models for the same test using $r_p = 50$ pixels.

From studying both Table 1 and Fig. 1, it can be seen that the recovered parameter values agree with the original values within their 1σ uncertainties. Interestingly, the rms scatter of the recovered model was found to be 499 ppm, while the rms scatter of the original model is 511 ppm. This showed that GEMC not only explored the large parameter search space but also scanned the local area around the global solution to find the best possible fit⁶ to the simulated data. This result is expected, and a testament to an optimization algorithm designed to find the lowest achievable χ^2_v (the recovered solution

⁶ This best fit is in fact a phantom solution generated by the addition of noise.

in this case had a $\chi^2_v = 0.94$) in a given parameter space. Similar results were found on all the simulation tests and show that both GEMC and PRISM are capable of accurately and precisely determining the properties of transit light curves.

The recovered parameter values from setting $r_p = 50$ and 15 pixels also agree within their 1σ uncertainties (see Table 1). The scale of the 1σ uncertainties for when $r_p = 15$ are comparable in scale to that of the 1σ uncertainties for when $r_p = 50$. This indicates that using a smaller number of pixels for the planetary radius (this reduction depends on the number of data points and the overall scale of the system being modelled) has little effect on the numerical resolution of the determined parameters or their associated uncertainties. However, using a smaller number of pixels for the planetary radius does affect the smoothness of the plotted best-fitting model. It is therefore advisable that, once the best-fitting parameters have been found, GEMC is used again with the parameters fixed at the best-fitting values and with $r_p = 50$ to calculate a smooth best-fitting model. These tests showed that it is possible to obtain precise results and correctly estimated parameter uncertainties, whilst, using a planetary pixel radius of less than 50. There are, though, some values which should not be used. For example, in tests using $r_p = 5$ the parameter uncertainties were heavily underestimated, due to numerical noise in the model. By making the planet only 10 pixels across, the numerical resolution decreases to the point where adverse effects can be seen in the results and uncertainties.

3 OBSERVATIONS AND DATA REDUCTION

Four transits of WASP-6 were observed on 2009/06/26, 2009/08/02, 2009/08/29 and 2010/07/31 by the MiNDSTeP consortium (Dominik et al. 2010) using the Danish 1.54-m telescope at ESO’s La Silla observatory in Chile. The instrument used was the Danish Faint Object Spectrograph and Camera imager, operated with a Bessell *R* filter. In this setup, the CCD covers a field of view of $(13.7 \text{ arcmin})^2$ with a pixel scale of $0.39 \text{ arcsec pixel}^{-1}$. The images were unbinned but windowed for faster readout, resulting in a dead time between consecutive images of between 22 and 35 s. The exposure times were 80–120 s. The Moon’s brightness and distance to the target star is given in Table 2. The telescope was defocused and autoguiding was maintained through all observations. The amount of defocus applied caused the resulting point spread functions to have a diameter of 86 pixels for the night of 2009/06/26, 32 pixels for the night of 2009/08/02, 44 pixels for the night of 2009/08/29 and 37 pixels for the night of 2010/07/31.

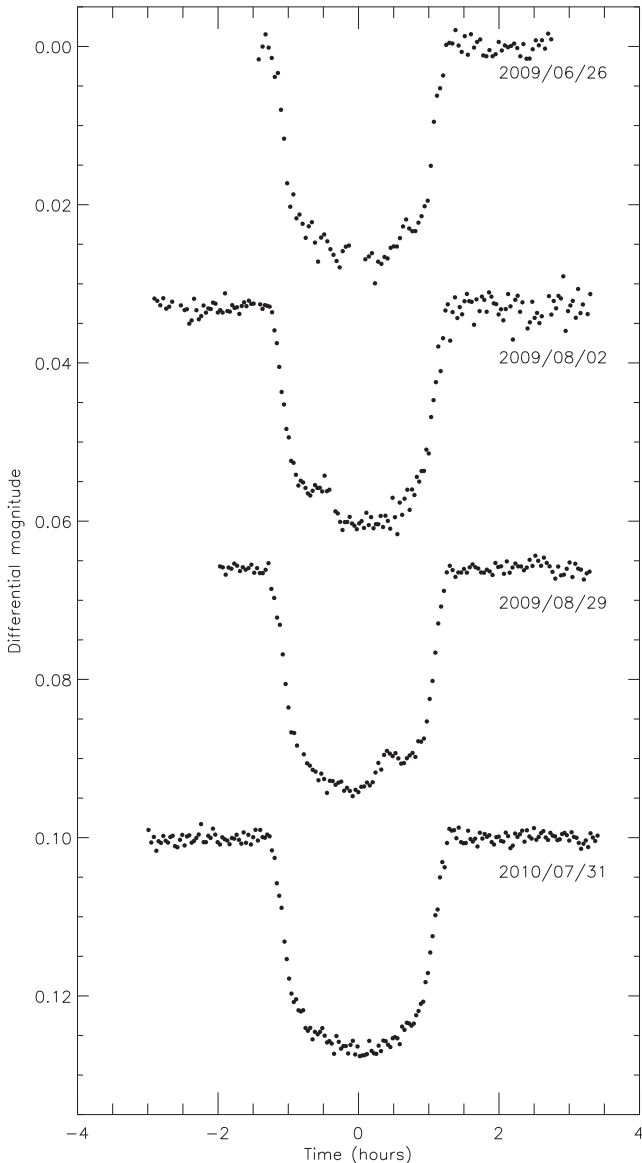
We reduced the data in an identical fashion to Southworth et al. (2009a,b). In short, aperture photometry was performed with an IDL implementation of DAOPHOT (Stetson 1987), and the aperture sizes were adjusted to obtain the best results (see Table 2). A first-order polynomial was then fitted to the outside-transit data whilst simultaneously optimizing the weights of the comparison stars. The resulting data have scatters ranging from 0.591 to 1.215 mmag per point versus a transit fit using PRISM. The timestamps from the fits files were converted to BJD/TDB. An observing log is given in Table 2 and the final light curves are plotted in Fig. 2.

4 DATA ANALYSIS

All four transits were modelled using PRISM and GEMC. To do this, a large parameter search space was selected to allow the global best-fitting solution to be found. As discussed in Tregloan-Reed et al. (2013), the ability of GEMC to find the global minimum in a short amount of computing time meant that it was possible to search a

Table 2. Log of the observations presented for WASP-6. N_{obs} is the number of observations. ‘Moon illum.’ and ‘Moon dist.’ are the fractional illumination of the Moon, and its angular distance from WASP-6 in degrees, at the mid-point of the transit.

Date	Start time (UT)	End time (UT)	N_{obs}	Exposure time (s)	Filter	Airmass	Moon illum.	Moon dist.	Aperture sizes (px)	Scatter (mmag)
2009/06/26	06:33	10:43	91	120	Bessell <i>R</i>	1.32 → 1.05	0.271	160.5	65, 90, 110	1.215
2009/08/02	04:18	10:31	175	90–120	Bessell <i>R</i>	1.28 → 1.44	0.934	59.6	27, 40, 70	0.939
2009/08/29	02:32	07:47	129	120	Bessell <i>R</i>	1.28 → 1.20	0.750	63.8	28, 40, 60	0.598
2010/07/31	03:51	10:20	193	80	Bessell <i>R</i>	1.45 → 1.34	0.686	42.4	25, 35, 55	0.591

**Figure 2.** The four light curves of WASP-6 presented in this work, in the order presented in Table 2. Times are given relative to the mid-point of each transit.

large area of parameter space to avoid the possibility of missing the best solution. The parameter search ranges used in analysing the WASP-6 data sets are given in Table 3. We modelled the two data sets containing a starspot anomaly independently, in order to obtain two sets of starspot parameters. This helps the investigation of whether the two anomalies are due to the same starspot (see Section 5).

The separate models of the four data sets of WASP-6 have parameters which are within 1σ of each other (Table 3). Ballerini et al. (2012) noted that starspots can affect the LD coefficients by up to 10 per cent in the *R* band. This is not seen in the WASP-6 data, unlike in the transit data of WASP-19 (Tregloan-Reed et al. 2013). The scatter around the weighted mean is $\chi^2_v = 0.149$ for the linear coefficient and 0.355 for the quadratic coefficient. The error bars on the LD coefficients are too large to allow the effects of starspots to be detected. This is due to the lower quality of the data compared to WASP-19 (Tregloan-Reed et al. 2013). The combined best-fitting LD coefficients are also in agreement within their 1σ uncertainties with the theoretically predicted values for WASP-6 A of $u_1 = 0.4125$ and $u_2 = 0.2773$ (Claret 2000).

4.1 Photometric results

The final photometric parameters for the WASP-6 system are given in Table 4 and are weighted means together with their 1σ uncertainties of the results from the four individual fits. Fig. 3 compares the light curves to the best-fitting models, including the residuals.

The available times of mid-transit for WASP-6 were collected from the literature (Gillon et al. 2009; Dragomir et al. 2011; Sada et al. 2012; Jordán et al. 2013; Nikolov et al. 2015). All timings were converted to the BJD/TDB time-scale and used to obtain an improved orbital ephemeris:

$$T_0 = \text{BJD/TDB } 2454425.02180(11) + 3.36100208(31) \times E,$$

where E represents the cycle count with respect to the reference epoch and the bracketed quantities represent the uncertainty in the final two digits of the preceding number. Fig. 4 and Table 5 show the residuals of these times against the ephemeris. The results show no evidence for transit timing variations.

Initially, we used the quoted mid-transit time from Gillon et al. (2009), but found that this value disagreed with the other 10 mid-transit times at the 2.2σ level. This may be because the value found by Gillon et al. (2009) was derived by simultaneously fitting the original WASP data plus two incomplete transits from RISE and a single complete transit from the FTS. We therefore used the same approach as Nikolov et al. (2015) and fitted (using PRISM) the archival FTS light curve to determine the mid-transit time. The value found using just the FTS data is in better agreement (0.6σ) with the other 10 mid-transit times. Therefore, it was decided to use the mid-transit time from the FTS light curve in our analysis, not just due to the better agreement but also due to the fact that it comes directly from a light curve covering a full transit.

4.2 Physical properties of the WASP-6 system

With the photometric properties of WASP-6 measured the physical characteristics could be determined. The analysis followed the method of Southworth (2009), which uses the parameters measured

Table 3. Derived photometric parameters from each light curve, plus the interval within which the best fit was searched for using GEMC.

Parameter	Search interval	2009/06/26	2009/08/02	2009/08/29	2010/07/31
Radius ratio	0.05–0.30	0.1443 ± 0.0055	0.1444 ± 0.0043	0.1474 ± 0.0017	0.1454 ± 0.0021
Sum of fractional radii	0.10–0.50	0.1102 ± 0.0060	0.1109 ± 0.0048	0.1115 ± 0.0025	0.1114 ± 0.0023
Linear LD coefficient	0.0–1.0	0.366 ± 0.119	0.397 ± 0.116	0.368 ± 0.077	0.402 ± 0.067
Quadratic LD coefficient	0.0–1.0	0.245 ± 0.191	0.325 ± 0.222	0.186 ± 0.123	0.192 ± 0.134
Orbital inclination (deg)	70.0–90.0	88.47 ± 0.99	88.55 ± 0.85	88.33 ± 0.48	88.36 ± 0.53
Transit epoch (BJD/TDB)	± 0.5 in phase	$2455\ 009.836\ 22 \pm 0.000\ 21$	$2455\ 046.80720 \pm 0.000\ 15$	$2455\ 073.695\ 29 \pm 0.000\ 13$	$2455\ 409.795\ 41 \pm 0.000\ 10$
Longitude of spot (deg)	–90 to +90		-26.15 ± 1.52	21.30 ± 0.99	
Colatitude of spot (deg)	0.0–90.0		78.76 ± 1.58	72.77 ± 1.12	
Spot angular radius (deg)	0.0–30.0		12.25 ± 1.40	12.17 ± 0.81	
Spot contrast	0.0–1.0		0.649 ± 0.187	0.798 ± 0.082	

Table 4. Combined system and spot parameters for WASP-6. The system parameters are the weighted means from all four data sets. The spot angular size and contrast are the weighted means from the two transits containing a starspot anomaly.

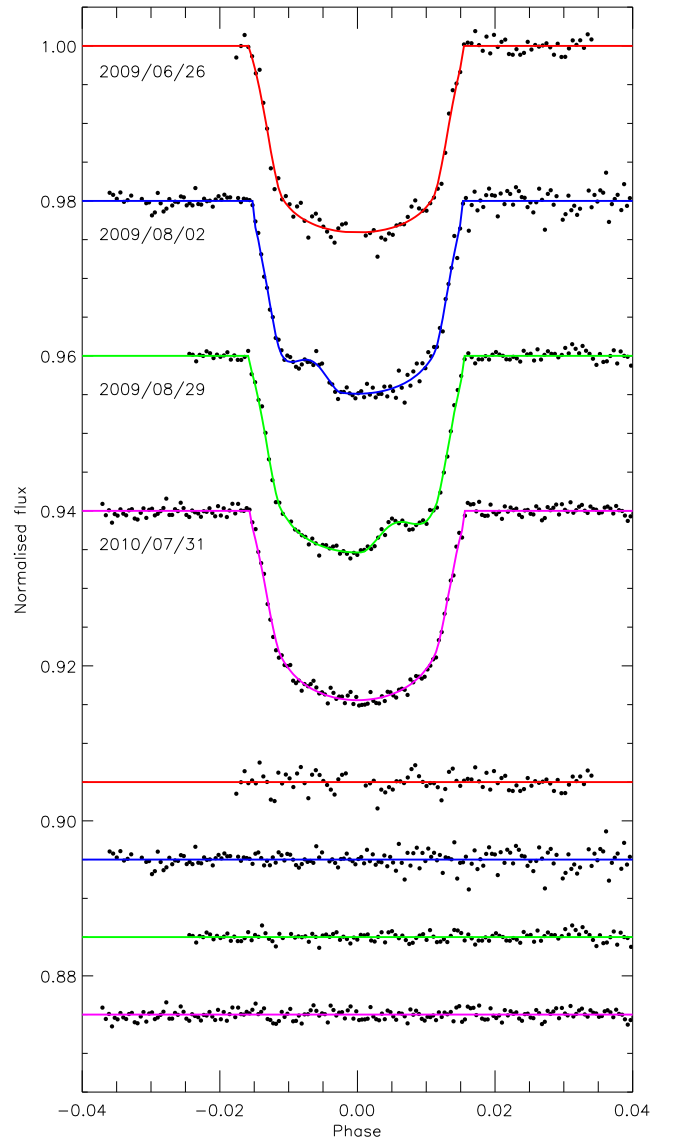
Parameter	Symbol	Value
Radius ratio	r_p/r_*	0.1463 ± 0.0012
Sum of fractional radii	$r_s + r_p$	0.1113 ± 0.0015
Linear LD coefficient	u_1	0.386 ± 0.043
Quadratic LD coefficient	u_2	0.214 ± 0.077
Orbital inclination (deg)	i	88.38 ± 0.31
Spot angular radius (deg)	r_{spot}	12.19 ± 0.70
Spot contrast	ρ_{spot}	0.774 ± 0.075
Stellar rotation period (d)	P_{rot}	23.80 ± 0.15
Projected spin orbit alignment (deg)	λ	7.2 ± 3.7

from the light curves and spectra, plus tabulated predictions of theoretical models. We adopted the values of i , r_p/r_* and $r_* + r_p$ from Table 4, the orbital velocity amplitude $K_* = 74.3^{+1.7}_{-1.4}$ m s⁻¹ and eccentricity $e = 0.054^{+0.018}_{-0.015}$ from Gillon et al. (2009), and the stellar effective temperature $T_{\text{eff}} = 5375 \pm 65$ K and metal abundance $[\text{Fe}/\text{H}] = -0.15 \pm 0.09$ from Doyle et al. (2013).

An initial value of the velocity amplitude of the planet, K_p , was used to calculate the physical properties of the system using standard formulae and the physical constants listed by Southworth (2011). The mass and $[\text{Fe}/\text{H}]$ of the star were then used to obtain the expected T_{eff} and radius, by interpolation within a set of tabulated predictions from theoretical stellar models. K_p was iteratively refined until the best agreement was found between the observed and expected T_{eff} , and the measured r_* and expected R_*/a . This was performed for ages ranging from the zero-age to the terminal-age main sequence, in steps of 0.01 Gyr. The overall best fit was found, yielding estimates of the system parameters and the evolutionary age of the star.

This procedure was performed separately using five different sets of stellar theoretical models (see Southworth 2010), and the spread of values for each output parameter was used to assign a systematic error. Statistical errors were propagated using a perturbation algorithm (see Southworth 2010).

The final results of this process are in reasonable agreement with themselves and with published results for WASP-6. The final physical properties are given in Table 6 and incorporate separate statistical and systematic error bars for those parameters which depend on the theoretical models. The final statistical error bar for each parameter is the largest of the individual ones from the solutions using each of the five different stellar models. The systematic error bar is the largest difference between the mean and the individual values of the parameter from the five solutions.


Figure 3. Transit light curves and the best-fitting models of WASP-6. The residuals are displayed at the base of the figure.

5 STARSPOT ANOMALIES

Two of the light curves, from 2009/08/02 and 2009/08/29, contain apparent starspot anomalies (see Fig. 2). Due to a 27-d gap between the two light curves, it is not possible to conclusively demonstrate that the anomalies are due to the same spot. But if so, the stellar rotation period and sky-projected spin orbit alignment can be

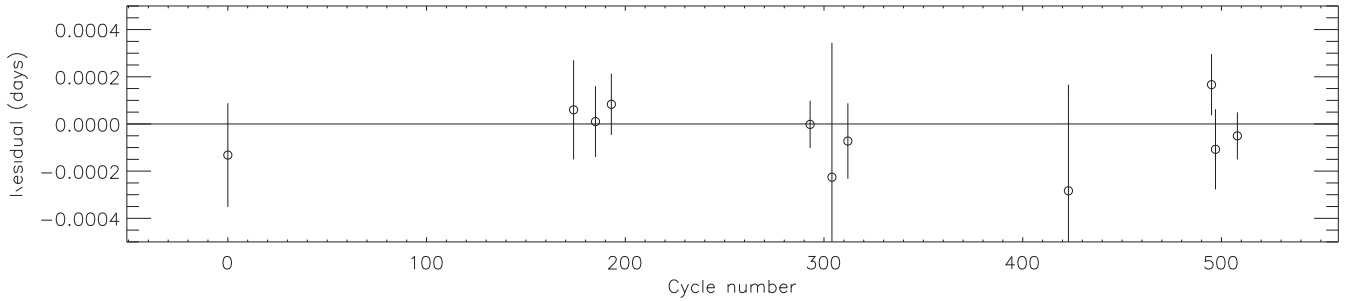


Figure 4. Residuals of the available times of mid-transit versus the orbital ephemeris found for WASP-6. The four timings from this work are the cluster of three points between the cycle numbers 170–200 and the point close to cycle 290.

Table 5. Times of minimum light of WASP-6 and their residuals versus the ephemeris derived in this work.

Time of minimum (BJD/TDB – 2400 000)	Cycle no.	Residual (BJD)	Reference
54425.02167 ± 0.00022	0.0	–0.00013	1
55009.83622 ± 0.00021	174.0	0.00006	2
55046.80720 ± 0.00015	185.0	0.00001	2
55073.69529 ± 0.00013	193.0	0.00008	2
55409.79541 ± 0.00010	293.0	–0.00000	2
55446.76621 ± 0.00058	304.0	–0.00023	3
55473.65438 ± 0.00016	312.0	–0.00007	4
55846.72540 ± 0.00045	423.0	–0.00028	5
56088.71800 ± 0.00013	495.0	0.00017	6
56095.43973 ± 0.00017	497.0	–0.00011	6
56132.41081 ± 0.00010	508.0	–0.00005	6

References: (1) Gillon et al. (2009); (2) this work; (3) Dragomir et al. (2011); (4) Jordán et al. (2013); (5) Sada et al. (2012); (6) Nikolov et al. (2015).

Table 6. Physical properties of the WASP-6 system. Where two error bars are given, the first is the statistical uncertainty and the second is the systematic uncertainty.

Parameter	Value
$M_A (M_\odot)$	$0.836 \pm 0.063 \pm 0.024$
$R_A (R_\odot)$	$0.864 \pm 0.024 \pm 0.008$
$\log g_A$ (cgs)	$4.487 \pm 0.017 \pm 0.004$
$\rho_A (\rho_\odot)$	1.296 ± 0.053
$M_b (M_{\text{Jup}})$	$0.485 \pm 0.027 \pm 0.009$
$R_b (R_{\text{Jup}})$	$1.230 \pm 0.035 \pm 0.012$
g_b (m s^{-2})	7.96 ± 0.30
$\rho_b (\rho_{\text{Jup}})$	$0.244 \pm 0.014 \pm 0.002$
T'_{eq} (K)	1184 ± 16
Θ	$0.0390 \pm 0.0014 \pm 0.0004$
a (au)	$0.0414 \pm 0.0010 \pm 0.0004$
Age (Gyr)	$9.0^{+8.0}_{-12.7} {}^{+4.0}_{-9.0}$

calculated and compared to the values found by Gillon et al. (2009), Doyle et al. (2013) and Nikolov et al. (2015). This will allow an indirect check on whether the two spot anomalies are due to the same starspot.

First, we consider whether the spot could last for a 27-d period. On the Sun, a spot’s lifetime T is proportional to its size A_0 following the Gnevyshev–Waldmeier (G-W) relation (Gnevyshev 1938; Waldmeier 1955):

$$A_0 = WT, \quad (2)$$

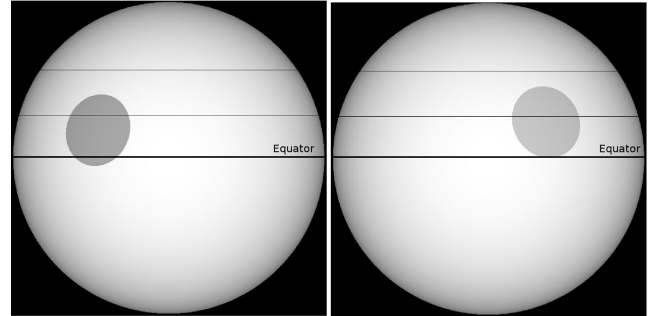


Figure 5. Representation of the stellar disc, starspot, transit chord and equator for the two data sets of WASP-6 containing spot anomalies. The axis of stellar rotation lies in the plane of the page and in the case of $\lambda = 0^\circ$ points upwards.

where A_0 is measured in MSH (micro-Solar hemispheres) and T is in days. Petrovay & van Driel-Gesztelyi (1997) state that $W = 10.89 \pm 0.18 \text{ MSH d}^{-1}$. Henwood, Chapman & Willis (2010) showed that large sunspots also followed the G-W relationship. If the same relationship is applied to starspots, then a minimum lifetime of 30 d requires a minimum size of 327 MSH, or an angular radius of just greater than 1° . Bradshaw & Hartigan (2014) argues that the standard solar G-W relation overestimates the lifetime of a starspot. Bradshaw & Hartigan (2014) uses turbulent magnetic diffusivity at supergranule size scales to calculate the magnetic diffusivity which in turn allows W in the G-W relation to be recalculated. Depending on the turbulent scalelength being used and to have a minimum lifetime of 30 d requires an angular radius of 3° – 9° (see fig. 1 Bradshaw & Hartigan 2014). The sizes of the starspot anomalies in the WASP-6 light curves are greater than 10° , so we conclude that a single spot can last sufficiently long to cause both anomalies, irrespective of the turbulent scalelength used.

5.1 Starspot anomalies results

The results from modelling the two spot anomalies suggest that they are due to the same spot rotating around the surface of the star, as the spot sizes and contrasts are in good agreement and the lifetime of a spot this size is much greater than the time interval between the two spotted transits. Fig. 5 is a representation of the stellar disc, the spot and the transit chord for the two nights of observations.

By assuming that the two spot anomalies are indeed caused by the same spot, it is straightforward to calculate the sky-projected spin orbit alignment of the system. We find a value of $\lambda = 7.2^\circ \pm 3.7^\circ$ from the measured positions of the starspot during the two transits.

It is also possible to calculate the rotational period of the star, using the spot positions and an estimate of the number of stellar rotations which occurred between the two transits (see Tregloan-Reed et al. 2013; Mancini et al. 2014). Due to the 27-d gap between the light curves, the star could have rotated N full rotations plus $47.5^\circ \pm 2.5^\circ$. If $N = 0$, then this would imply that WASP-6 has a rotation period of approximately 200 d, which is extremely long for a main-sequence G-star. If $N = 1$, then the spot has travelled $407.5^\circ \pm 2.5^\circ$ between the transits, giving a rotational period of $P_{\text{rot}} = 23.80 \pm 0.15$ d at a colatitude of 75.8° . This is in excellent agreement with the measurement of $P_{\text{rot}} = 23.6 \pm 0.5$ d from Nikolov et al. (2015). Combining this with the stellar radius (see Table 6), the latitudinal rotational velocity of the star was calculated to be $v_{(75.8^\circ)} = 1.78 \pm 0.20$ km s $^{-1}$. This is also in agreement with $v \sin I$ from both Gillon et al. (2009) and Doyle et al. (2013). If $N = 2$, then the spot has travelled $767.5^\circ \pm 2.5^\circ$, giving a rotational period of $P_{\text{rot}} = 12.63 \pm 0.15$ d at a colatitude of 75.8° (or $v_{(75.8^\circ)} = 3.36 \pm 0.20$ km s $^{-1}$). This agrees with the $v \sin I$ from Gillon et al. (2009) and Doyle et al. (2013), but not with the P_{rot} from Nikolov et al. (2015). The agreement with Gillon et al. (2009) and Doyle et al. (2013) is due to the fact that any value of v that is found to be greater than $v \sin I$ can be considered to agree based on the nature of $\sin I$. We conclude that the $N = 1$ case is much more likely than the two alternatives discussed above.

5.2 Degeneracy of the stellar rotation period

Whilst there is no clear photometric signal in the SuperWASP light curve of WASP-6, Nikolov et al. (2015) were able to measure a rotation period of $P_{\text{rot}} = 23.6 \pm 0.5$ d from photometry of higher precision; however, none of the Space Telescope Imaging Spectrograph observations detected a starspot anomaly indicating that starspots on WASP-6 A are either rare or of low contrast. This is also supported by the upper limit of the photometric variability of about 1 per cent (Nikolov et al. 2015). There are also two measurements of $v \sin I$ from Gillon et al. (2009, $v \sin I = 1.4 \pm 1.0$ km s $^{-1}$) and Doyle et al. (2013, $v \sin I = 2.4 \pm 0.5$ km s $^{-1}$). Both $v \sin I$ measurements agree with the v found when combining P_{rot} and R_* at a colatitude of 75.8° to give either $v_{(75.8^\circ)} = 1.78 \pm 0.20$ km s $^{-1}$ or $v_{(75.8^\circ)} = 3.36 \pm 0.20$ km s $^{-1}$. The problem that arises from checking measurements of v against $v \sin I$ is that due to the $\sin I$ projection factor any value for v that is found to be greater than $v \sin I$ can be considered to agree. A second unknown is the amount of differential rotation that is experienced by WASP-6 A. In the absence of any differential rotation, the single full rotation value of $P_{\text{rot}} = 23.80 \pm 0.15$ d would lead to an equatorial rotational velocity of $v = 1.84 \pm 0.20$ km s $^{-1}$. This result agrees again with the $v \sin I$ value from both Gillon et al. (2009) and Doyle et al. (2013). Our results from PRISM do show though that the two starspot positions are only approximately 10° from the stellar equator. As such the effect from differential rotation would be small, so any large divergence of v from $v \sin I$ would imply that $I < 90^\circ$.

WASP-6 A has $T_{\text{eff}} = 5375 \pm 65$ K (Doyle et al. 2013) so is a cool star ($T_{\text{eff}} < 6250$ K). The trend seen between host star T_{eff} s and projected orbital obliquity (see Fig. 6) suggests that the orbital rotation axis of WASP-6 b should be aligned with the stellar rotation axis of WASP-6 A. For this to be true, then I would have to be $\approx 90^\circ$, and thus $\sin I \approx 1$. If this is the case, then the value $v_{(75.8^\circ)} = 3.36 \pm 0.20$ km s $^{-1}$ no longer agrees with the $v \sin I$ from either Gillon et al. (2009) or Doyle et al. (2013). This supports the supposition that the rotation period of WASP-6 A is $P_{\text{rot}} = 23.80 \pm 0.15$ d. Brown (2014) calculated the stellar rotation period of WASP-6 A to

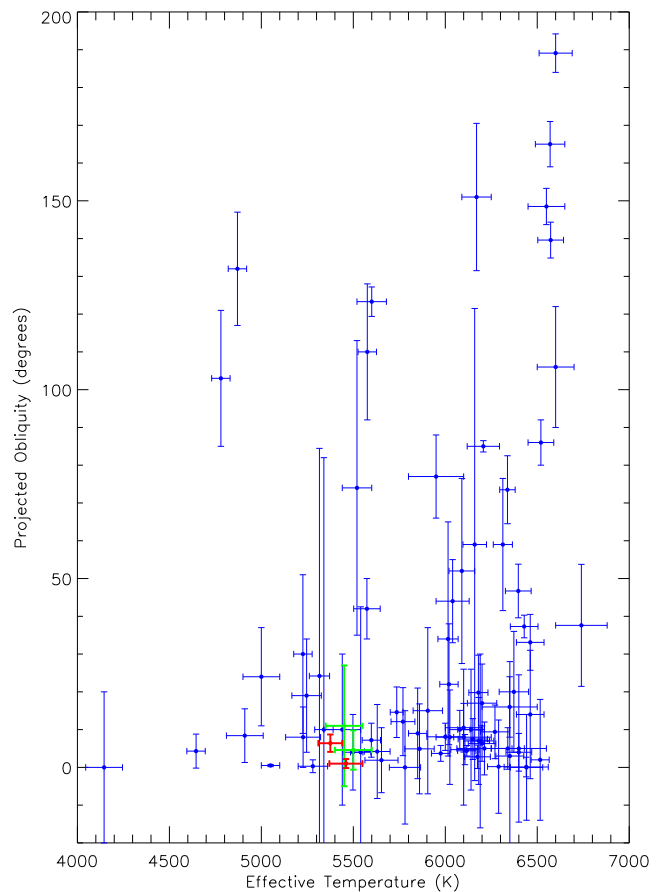


Figure 6. $|\lambda|$ against T_{eff} for 83 transiting planets from TEPcat including WASP-19 and WASP-6. The green and red data points are WASP-6 (left) and WASP-19 (right). The green data points represent values from the literature (WASP-6: Gillon et al. 2009; WASP-19: Hellier et al. 2011) and the red data points represent the values found from this work and Tregloan-Reed et al. (2013). The trend in the data suggests that cool host stars harbour aligned systems.

be $P_{\text{rot}} = 27.1^{+3.6}_{-3.8}$ d from Gaussian distribution sampling of $v \sin I$, i and R_A , which is further evidence for the conclusion that the rotation period of WASP-6 A is $P_{\text{rot}} = 23.80 \pm 0.15$ d.

6 DISCUSSION AND CONCLUSIONS

We have determined the physical properties of the WASP-6 planetary system (Table 6) based on four new high-precision transit light curves, finding values which are consistent with and more precise than those in the literature. We find the mass and radius of the host star to be $0.836 \pm 0.063 M_\odot$ and $0.864 \pm 0.024 R_\odot$, respectively. For the planet we find a mass of $0.485 \pm 0.027 M_{\text{Jup}}$, a radius of $1.230 \pm 0.035 R_{\text{Jup}}$ and a density of $0.244 \pm 0.014 \rho_{\text{Jup}}$. These results also serve as a secondary check for the accuracy of the PRISM and GEMC codes. By studying the individual results for each of the four transits (see Table 3), it can be seen that the system parameters from each light curve agree within their 1σ uncertainties. This shows that PRISM can retrieve reliable photometric properties from transit light curves containing starspot anomalies.

The four transits of WASP-6 were modelled using PRISM and GEMC. Two of the transits contained a starspot anomaly but are separated by

27 d. Whilst it is not possible to prove that the two spot anomalies are caused by the same starspot, the available evidence strongly favours this scenario. The results from PRISM show that the angular size and contrast of the starspot in both light curves agree to within 0.05σ and 0.73σ , respectively. As with WASP-19 (see Tregloan-Reed et al. 2013), only part of the starspot(s) is on the transit chord (Fig. 5). Because the light curve only holds information on what is happening inside the transit chord, then a likely scenario is that the planet is passing over a band of smaller starspots which form an active region on WASP-6. In this active region, there could be a number of starspots each with sizes much less than 1° and therefore lifetimes shorter than 30 d (see Section 5). Future observations may allow changes to be seen in the overall contrast from the starspot region. In either case as a whole the region would remain a similar size and shape over a 27-d period.

In the case of a single large starspot, r_{spot} (Table 4) and R_* (Table 6) can be combined to find the starspot radius. We find $R_{\text{spot}} = 127902 \pm 11102$ km, which equates to approximately 4.5 per cent of the visible stellar surface. This value is similar to starspots found on other G-type stars (Strassmeier 2009).

If the two starspot anomalies are assumed to be generated by the planet crossing the same starspot, then it is possible to calculate the latitudinal rotation period of WASP-6. It was found that either $P_{\text{rot}} = 23.80 \pm 0.15$ d or $P_{\text{rot}} = 12.63 \pm 0.15$ d at a colatitude of 75.8° . These calculations assumed that WASP-6 had made either one or two full rotations prior to the difference seen in the light curves.

Even without knowing the number of full rotations that WASP-6 completed between the two spotted light curves, if the starspot anomalies are due to the same spot then the sky-projected spin orbit alignment λ of the system can be measured. We find $\lambda = 7.2^\circ \pm 3.7^\circ$. This result agrees with, and is more precise than, the previous measurement of λ using the RM effect ($\lambda = 11^{+14}_{-18}$ deg; Gillon et al. 2009). λ gives the lower boundary of the true spin-orbit angle, ψ . As stated by Fabrycky & Winn (2009), finding a small value for λ can be interpreted in different ways. Either ψ lies close to λ and the system is aligned, or ψ lies far from λ and the system is not aligned. As discussed in Section 5.1 because the spot is close to the stellar equator, then it could be assumed that the change in v at the equator due to differential rotation would be small. Coupled with the uncertainties measured in $v \sin I$ from both Gillon et al. (2009) and Doyle et al. (2013), it is plausible that $\sin I \approx 1$ and therefore $\psi \approx 7^\circ$ if $P_{\text{rot}} = 23.80 \pm 0.15$ d. As a consequence, we have two different scenarios: an aligned system with a slowly rotating star or a misaligned system with a rapidly rotating star. Taking into account the T_{eff} of WASP-6 A and the statistical trend seen in misaligned systems, it is more probable that the WASP-6 system is in fact aligned, suggesting $\psi \approx 7^\circ$ and $P_{\text{rot}} = 23.80 \pm 0.15$ d. It would be desirable to observe consecutive transits of WASP-6 in an attempt to definitively identify multiple planetary crossings of a single starspot and to precisely determine P_{rot} , λ and potentially ψ of WASP-6.

If the starspot anomalies are due to the same starspot, $\lambda = 7.2^\circ \pm 3.7^\circ$ and there is no direct evidence for a spin-orbit misalignment in the WASP-6 system. With potentially a low obliquity and a cool host star, WASP-6 seems to follow the idea put forward by Winn et al. (2010a) that planetary systems with cool stars will have a low obliquity. It also lends weight to the idea that WASP-6 b formed at a much greater distance from its host star and suffered orbital decay through tidal interactions with the protoplanetary disc (i.e. either type I or type II disc migration; Ward 1997).

At present there are 83 transiting planets with published λ values.⁷ The λ values for WASP-6 (this work) and WASP-19 (Tregloan-Reed et al. 2013) were updated and a plot of λ against T_{eff} was created (see Fig. 6). To remove any ambiguity in the plot due to negative values of λ , we plot its absolute value. It can be seen that a large proportion (75 per cent) of cool stars ($T_{\text{eff}} < 6250$ K) are in aligned systems, while the majority (56 per cent) of hot host stars have misaligned systems. This trend supports Winn et al. (2010a) in that cool stars with hot Jupiters will have low obliquities. This trend can also be explained by the time required for the system to align. Hot stars will have thinner convective zones and will therefore take longer to align the photosphere with the planetary orbit. Because of this, by examining λ of hot stars a greater proportion will have misaligned systems compared to cool stars where the alignment process is much shorter and so will have a higher proportion of aligned systems. Cool stars also live longer so the ones that are observed are on average older. They have therefore had more time for tidal effects to work (Triaud 2011).

By determining λ and ψ of the planetary system, it is possible to begin to understand the primary process in the dynamical evolution of the system. The RM effect can be used to ascertain a value for λ . One limitation of this method though is from an excess RV jitter (stellar activity e.g. starspots). Therefore, the use of the RM effect either requires magnetically quiet stars or the transit chord of the planet to bypass any active latitudes on the stellar disc. The opposite is true when using starspot anomalies in light curves to determine λ . Due to this, the two different methods complement each other in probing the dominant process in the dynamical evolution of transiting planets. It should be noted that in both the cases of WASP-19 and WASP-6 (see Fig. 6) the measured uncertainty in λ is much smaller than measured using the RM effect. This indicates that the starspot method to measure λ is superior to the RM effect in terms of reduced uncertainty in measuring λ . However, as was shown in observing WASP-50 (see Tregloan-Reed & Southworth 2013), the starspot method does not always work in terms of obtaining transit light curves affected by a starspot anomaly. The RM effect does have a high success rate in measuring a value of λ but rarely achieves a similar precision.

ACKNOWLEDGEMENTS

We like to thank the anonymous referee for the helpful comments on the manuscript. The operation of the Danish 1.54-m telescope at ESOs La Silla observatory is financed by a grant to UGJ from The Danish Council for Independent Research (FNU). Research at the Armagh Observatory is funded by the Department of Culture, Arts & Leisure (DCAL). JTR acknowledges financial support from STFC in the form of a PhD Studentship (the majority of this work) and also acknowledges financial support from ORAU (Oak Ridge Associated Universities) and NASA in the form of a Post-Doctoral Programme (NPP) Fellowship. JS acknowledges financial support from STFC in the form of an Advanced Fellowship. DR acknowledges financial support from the Spanish Ministry of Economy and Competitiveness (MINECO) under the 2011 Severo Ochoa Programme MINECO SEV-2011-0187. FF, DR (boursier FRIA) and J Surdej acknowledge support from the Communauté française de Belgique – Actions de recherche concertées – Académie Wallonie–Europe.

⁷ All measured λ and T_{eff} values of the known planetary systems were obtained from the 2014/10/20 version of the TEPcat catalogue (Southworth 2011) (<http://www.astro.keele.ac.uk/~jkt/tepcat/>).

REFERENCES

- Baglin A. et al., 2006, in 36th COSPAR Scientific Assembly, CoRoT: A High Precision Photometer for Stellar Evolution and Exoplanet Finding. p. 3749
- Bakos G., Noyes R. W., Kovács G., Stanek K. Z., Sasselov D. D., Domsa I., 2004, *PASP*, 116, 266
- Ballerini P., Micela G., Lanza A. F., Pagano I., 2012, *A&A*, 539, A140
- Baranne A. et al., 1996, *A&AS*, 119, 373
- Barros S. C. C., Boué G., Gibson N. P., Pollacco D. L., Santerne A., Keenan F. P., Skillen I., Street R. A., 2013, *MNRAS*, 430, 3032
- Béky B., Kipping D. M., Holman M. J., 2014, *MNRAS*, 442, 3686
- Borucki W. J. et al., 2010, *Science*, 327, 977
- Borucki W. J. et al., 2012, *ApJ*, 745, 120
- Borucki W. J. et al., 2013, *Science*, 340, 587
- Bradshaw S. J., Hartigan P., 2014, *ApJ*, 795, 79
- Brown D. J. A., 2014, *MNRAS*, 442, 1844
- Butler R. P., Marcy G. W., Williams E., McCarthy C., Dossanjh P., Vogt S. S., 1996, *PASP*, 108, 500
- Butler R. P., Marcy G. W., Fischer D. A., Brown T. M., Contos A. R., Korzennik S. G., Nisenson P., Noyes R. W., 1999, *ApJ*, 526, 916
- Carter J. A., Winn J. N., Holman M. J., Fabrycky D., Berta Z. K., Burke C. J., Nutzman P., 2011, *ApJ*, 730, 82
- Claret A., 2000, *A&A*, 363, 1081
- Désert J.-M. et al., 2011, *ApJS*, 197, 14
- Dominik M. et al., 2010, *Astron. Nachr.*, 331, 671
- Doyle L. R. et al., 2011, *Science*, 333, 1602
- Doyle A. P. et al., 2013, *MNRAS*, 428, 3164
- Dragomir D. et al., 2011, *ApJ*, 142, 115
- Fabrycky D. C., Winn J. N., 2009, *ApJ*, 696, 1230
- Gelman A., Rubin R., 1992, *Stat. Sci.*, 7, 457
- Gillon M. et al., 2009, *A&A*, 501, 785
- Gnevyshv M. N., 1938, *Izv. Gl. Astron. Obs. Pulkove*, 16, 36
- Hellier C., Anderson D. R., Collier-Cameron A., Miller G. R. M., Queloz D., Smalley B., Southworth J., Triaud A. H. M. J., 2011, *ApJ*, 730, L31
- Henwood R., Chapman S. C., Willis D. M., 2010, *Solar Phys.*, 262, 299
- Jordán A. et al., 2013, *ApJ*, 778, 184
- Kipping D. M., Dunn W. R., Jasinski J. M., Manthri V. P., 2012, *MNRAS*, 421, 1166
- Maciejewski G., Raetz S., Nettelmann N., Seeliger M., Adam C., Nowak G., Neuhäuser R., 2011, *A&A*, 535, A7
- Mancini L. et al., 2013, *MNRAS*, 436, 2
- Mancini L. et al., 2014, *MNRAS*, 443, 2391
- Mayor M. et al., 2003, *The Messenger*, 114, 20
- Mohler-Fischer M. et al., 2013, *A&A*, 558, A55
- Nikolov N. et al., 2015, *MNRAS*, 447, 463
- Nutzman P. A., Fabrycky D. C., Fortney J. J., 2011, *ApJ*, 740, L10
- Orosz J. A. et al., 2012, *Science*, 337, 1511
- Petrovay K., van Driel-Gesztelyi L., 1997, *Solar Phys.*, 176, 249
- Pollacco D. L. et al., 2006, *PASP*, 118, 1407
- Pont F. et al., 2007, *A&A*, 476, 1347
- Price K., Storn R., 1997, *Dr. Dobbs's J.*, 264, 18
- Queloz D. et al., 2000, *A&A*, 354, 99
- Rabus M. et al., 2009, *A&A*, 494, 391
- Sada P. V. et al., 2012, *PASP*, 124, 212
- Sanchis-Ojeda R., Winn J. N., 2011, *ApJ*, 743, 61
- Sanchis-Ojeda R., Winn J. N., Holman M. J., Carter J. A., Osip D. J., Fuentes C. I., 2011, *ApJ*, 733, 127
- Schneider J., Dedieu C., Le Sidaner P., Savalle R., Zolotukhin I., 2011, *A&A*, 532, A79
- Schwamb M. E. et al., 2013, *ApJ*, 768, 127
- Silva A. V. R., 2003, *ApJ*, 585, L147
- Silva-Valio A., Lanza A. F., Alonso R., Barge P., 2010, *A&A*, 510, A25
- Southworth J., 2009, *MNRAS*, 394, 272
- Southworth J., 2010, *MNRAS*, 408, 1689
- Southworth J., 2011, *MNRAS*, 417, 2166
- Southworth J. et al., 2009a, *MNRAS*, 396, 1023
- Southworth J. et al., 2009b, *MNRAS*, 399, 287
- Steele I. A., Bates S. D., Gibson N., Keenan F., Meaburn J., Mottram C. J., Pollacco D., Todd I., 2008, in McLean I. S., Casali M. M., eds, *Proc. SPIE Conf. Ser. Vol. 7014, Ground-based and Airborne Instrumentation for Astronomy II*. SPIE, Bellingham, p. 6
- Stetson P. B., 1987, *PASP*, 99, 191
- Storn R., Price K., 1997, *J. Global Optimisation*, 11, 341
- Strassmeier K. G., 2009, *A&AR*, 17, 251
- Ter Braak C. J. F., 2006, *Stat. Comput.*, 16, 239
- Tregloan-Reed J., Southworth J., 2013, *MNRAS*, 431, 966
- Tregloan-Reed J., Southworth J., Tappert C., 2013, *MNRAS*, 428, 3671
- Triaud A. H. M. J., 2011, *A&A*, 534, L6
- Waldmeier M., 1955, *Leipzig, Geest & Portig*, 1955. 2. erweiterte Aufl.
- Ward W. R., 1997, *Icarus*, 126, 261
- Welsh W. F. et al., 2012, *Nature*, 481, 475
- Winn J. N., Fabrycky D., Albrecht S., Johnson J. A., 2010a, *ApJ*, 718, L145
- Winn J. N. et al., 2010b, *ApJ*, 723, L223
- ¹NASA Ames Research Center, Moffett Field, CA 94035, USA
- ²Astrophysics Group, Keele University, Staffordshire ST5 5BG, UK
- ³Universität Hamburg Meteorologisches Institut Bundesstraße 55 D-20146 Hamburg, Germany
- ⁴NASA Exoplanet Science Institute, MS 100-22, California Institute of Technology, Pasadena, CA 91125, USA
- ⁵Dipartimento di Fisica 'E.R. Caianiello', Università di Salerno, Via Giovanni Paolo II 132, I-84084 Fisciano (SA), Italy
- ⁶Istituto Internazionale per gli Alti Studi Scientifici (IIASS), I-84019 Vietri Sul Mare (SA), Italy
- ⁷SUPA, University of St Andrews, School of Physics & Astronomy, North Haugh, St Andrews, Fife KY16 9SS, UK
- ⁸Institut d'Astrophysique et de Géophysique, Université de Liège, B-4000 Liège, Belgium
- ⁹Aryabhata Research Institute of Observational Sciences (ARIES), Manora Peak, Nainital 263 129, Uttarakhand, India
- ¹⁰Niels Bohr Institute & Centre for Star and Planet Formation, University of Copenhagen, Østervoldgade 5, DK-1350 Copenhagen K, Denmark
- ¹¹Astronomisches Rechen-Institut, Zentrum für Astronomie, Universität Heidelberg, Mönchhofstraße 12-14, D-69120 Heidelberg, Germany
- ¹²Max Planck Institute for Astronomy, Königstuhl 17, D-69117 Heidelberg, Germany
- ¹³Observatorio Astronómico Nacional, Instituto de Astronomía – Universidad Nacional Autónoma de México, Ap. P. 877, Ensenada, BC 22860, Mexico
- ¹⁴Instituto de Astrofísica de Canarias, E-38205 La Laguna, Tenerife, Spain
- ¹⁵Departamento de Astrofísica, Universidad de La Laguna, E-38206 La Laguna, Tenerife, Spain
- ¹⁶Planetary and Space Sciences, Department of Physical Sciences, The Open University, Milton Keynes MK7 6AA, UK
- ¹⁷Istituto Nazionale di Fisica Nucleare, Sezione di Napoli, I-80126 Napoli, Italy
- ¹⁸Korea Astronomy and Space Science Institute, Daejeon 305-348, Republic of Korea
- ¹⁹Armagh Observatory, College Hill, Armagh BT61 9DG, UK
- ²⁰Space Telescope Science Institute, 3700 San Martin Drive, Baltimore, MD 21218, USA
- ²¹Jodrell Bank Centre for Astrophysics, University of Manchester, Oxford Road, Manchester M13 9PL, UK
- ²²Department of Astronomy, Ohio State University, 140 W. 18th Ave., Columbus, OH 43210, USA
- ²³Department of Physics, Sharif University of Technology, PO Box 11155-9161 Tehran, Iran
- ²⁴Institut für Astrophysik, Georg-August-Universität Göttingen, Friedrich-Hund-Platz 1, D-37077 Göttingen, Germany

This paper has been typeset from a $\text{\TeX}/\text{\LaTeX}$ file prepared by the author.